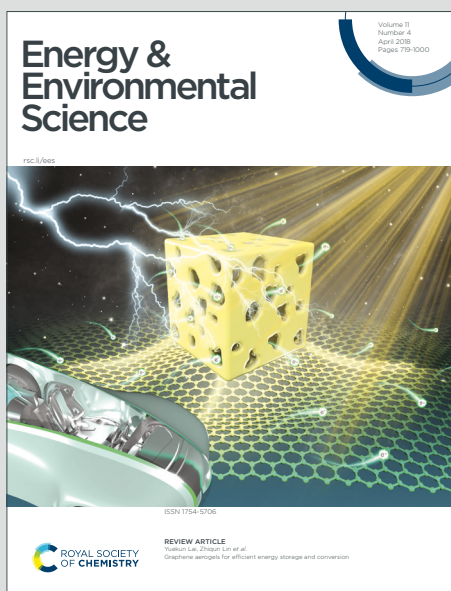


Energy & Environmental Science

Accepted Manuscript

This article can be cited before page numbers have been issued, to do this please use: Y. Wang, H. Hong, Z. Wei, D. Li, X. Yang, J. Zhu, P. Li, S. Wang and C. Zhi, *Energy Environ. Sci.*, 2025, DOI: 10.1039/D4EE03385J.



This is an Accepted Manuscript, which has been through the Royal Society of Chemistry peer review process and has been accepted for publication.

Accepted Manuscripts are published online shortly after acceptance, before technical editing, formatting and proof reading. Using this free service, authors can make their results available to the community, in citable form, before we publish the edited article. We will replace this Accepted Manuscript with the edited and formatted Advance Article as soon as it is available.

You can find more information about Accepted Manuscripts in the [Information for Authors](#).

Please note that technical editing may introduce minor changes to the text and/or graphics, which may alter content. The journal's standard [Terms & Conditions](#) and the [Ethical guidelines](#) still apply. In no event shall the Royal Society of Chemistry be held responsible for any errors or omissions in this Accepted Manuscript or any consequences arising from the use of any information it contains.

Broader context statement

Zinc-manganese batteries are typically dry cells that can be bought from supermarkets. The evolution from non-rechargeable zinc-manganese dry cells to zinc-manganese flow batteries (Zn-Mn FBs) signifies a crucial step towards scalable and sustainable energy storage. Here, we realize Zn-Mn FBs with high reversibility (2600 cycles) and energy density (38.2 mWh cm⁻² per cycle and 23.75 Wh cm⁻² cumulatively). This work propels the transition of traditional supermarket zinc-manganese batteries to flow systems for large-scale energy storage.



View Article Online
DOI: 10.1039/D4EE03385J

Cation-regulated MnO₂ Reduction Reaction Enabling Long-term Stable Zinc-Manganese Flow Batteries with High Energy Density

*Yiqiao Wang¹, Hu Hong¹, Zhiquan Wei¹, Dedi Li¹, Xinru Yang¹, Jiaxiong Zhu¹, Pei Li¹, Shengnan Wang¹ and Chunyi Zhi^{*1}*

¹Department of Materials Science and Engineering, City University of Hong Kong, 83 Tat Chee Avenue, Kowloon, Hong Kong 999077, China

*Corresponding Author

E-mail: cy.zhi@cityu.edu.hk (C. Zhi)



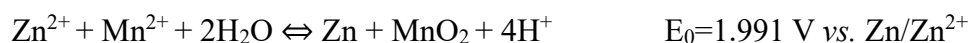
Abstract

Aqueous Zn-Mn flow batteries (Zn-Mn FBs) are a potential candidate for large-scale energy storage due to their high voltage, low cost, and environmental friendliness. However, the unsatisfactory performance due to the sluggish MnO₂ reduction reaction (MnRR) kinetics leads to low discharge voltage (typically < 1.7 V) and poor stability (typically < 1000 cycles), which hinders their practical application. Here, we successfully achieve a reversible Mn²⁺/MnO₂ reaction by a cation-regulated MnO₂ formation/decomposition process. The dual role of Mg²⁺ addition in locking free water and forming Mg-doped MnO₂ compounds with enlarged atomic spacing was revealed, leading to excellent electrolyte stability and highly reversible MnRR. The Zn-Mn FBs with Mg²⁺ exhibit a high discharge voltage of 1.91 V at 20 mA cm⁻² and superior long-term stability for over 2600 cycles, thus realizing a considerably high energy density (38.2 mWh cm⁻² per cycle and 23.75 Wh cm⁻² cumulatively). This work underscores the importance of electrolyte engineering to the reversibility of Mn-based reactions and its potential for high power and energy density applications.



Introduction

Aqueous flow batteries (AFBs) have attracted much interest due to their high safety, flexible design, and long cycling stability, making them suitable for energy storage devices for harvesting renewable intermittent energy such as solar and wind¹⁻³. Zinc-manganese flow batteries (Zn-Mn FBs) present distinct advantages over other types of flow batteries, such as all-vanadium (VFBS), zinc-bromine (Zn-Br₂ FBs), and aqueous organic (AORFBs) due to their high voltage achieved through the Mn²⁺ to MnO₂ reaction, cost-effectiveness, abundance of element, and environmental friendliness⁴⁻⁶. These features position Zn-Mn batteries as an up-and-coming option in energy storage. Manganese chemistry based on a conversion mechanism has been initially implemented in the flow battery systems⁷⁻¹². When paired with the zinc anode, a high theoretical voltage ($E_0=1.991$ V) and substantial specific capacity of 616 mAh g⁻¹_{MnO₂} can be potentially achieved^{11,13-15}. The reaction formula is delineated as follows:



As shown in Figure 1a of the typical reaction process of Zn-Mn FBs, the oxidation of Mn²⁺ to MnO₂ transpires at the cathode, concurrently with Zn²⁺ reduction at the anode in the charging sequence. This transformation process of active substance from liquid to solid phase in charging (Figure 1b,1) and conversely dissolution back into the electrolyte during discharge suffers from sluggish kinetics due to the poor electrical conductivity of electrodeposited MnO₂^{4,14,16}. The incomplete decomposition of MnO₂ during discharging in conventional acidic Mn-based catholytes leads to the accumulation of MnO₂ solids, passivating the cathode and forming "dead Mn" (Figure 1b,2) as the products are flushed by electrolyte flow, thereby lowering the discharge voltage, capacity and cycling stability, and restricting the energy density of Zn-Mn FBs.



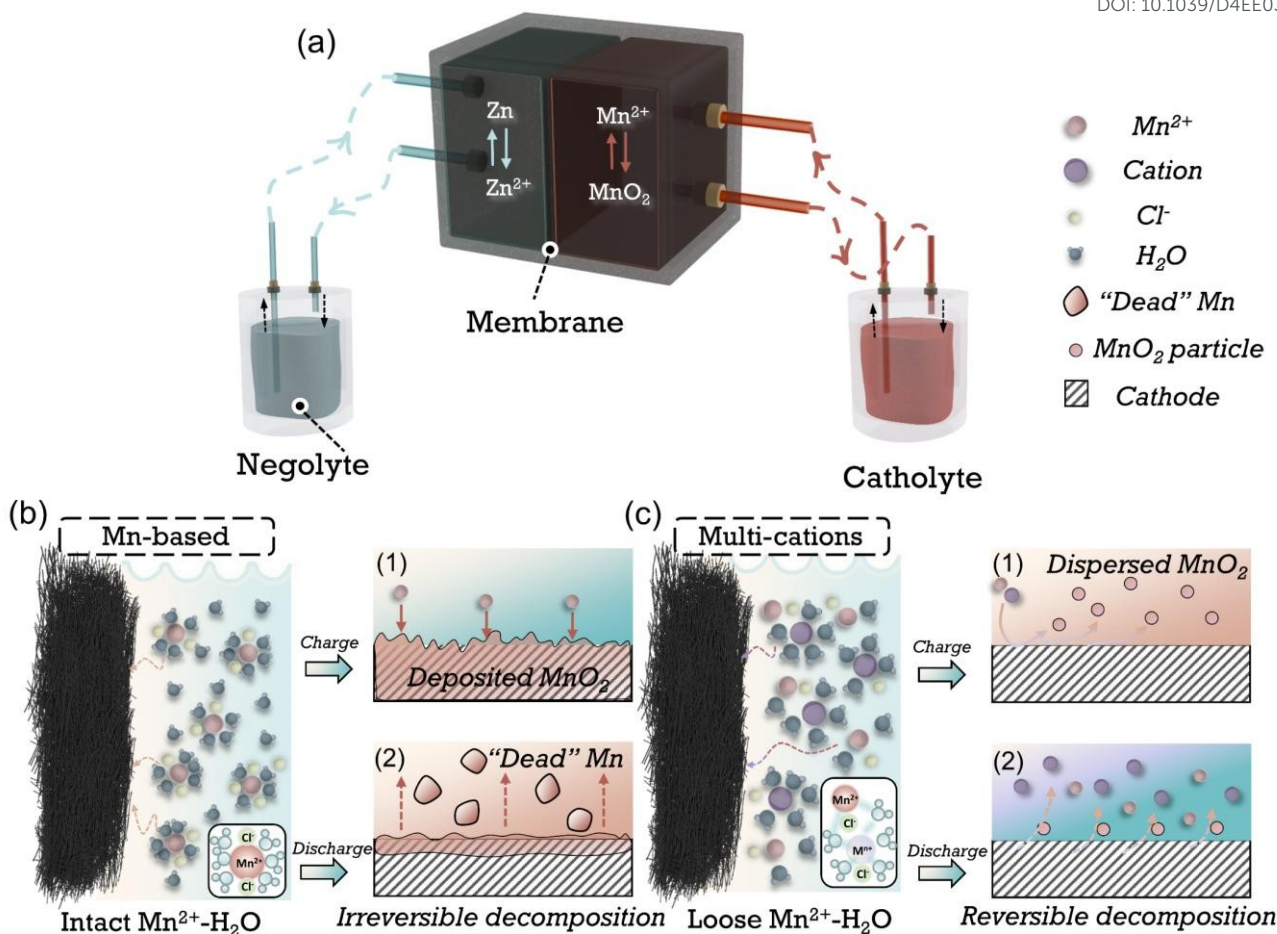
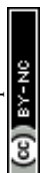


Figure 1. Schematic of the reaction process of the Zn-Mn flow batteries.

(a) shows a Zn-Mn flow battery device. The following magnified chart shows the solvation structure of cation in (b) conventional Mn-based and (c) multi-cationic catholytes, respectively. MnO₂ deposition and irreversible decomposition process in Mn-based electrolytes during (b,1) charging and (b,2) discharging. Formation of MnO₂ dispersion and reversible decomposition process in multi-cationic electrolytes during (c,1) charging and (c,2) discharging.

Many efforts have been made to improve the reversibility of manganese conversion reactions to improve stability while augmenting the capacity or voltage. Through utilizing the coordination effect of anions with Mn²⁺, e.g., acetate, Ethylenediaminetetraacetic acid (EDTA), reversibility can be amended by inhibiting the disproportionation of the Mn³⁺ intermediates and avoiding the formation of



"dead Mn"^{10,17,18}. The acetate-based electrolytes have demonstrated significantly improved cycling stability in flow batteries.^{9,11} Nevertheless, the diminished proton activity in mild electrolytes and alterations in the coordination structure yields a reduced discharge voltage (<1.6 V vs. Zn/Zn²⁺). Moreover, the impaired compatibility of zinc anode in acetate electrolytes leads to limited stability, especially at high areal capacity^{19,20}. An alternative approach involves employing decoupled electrolytes, achieved using acidic and alkaline-based electrolytes as catholytes and anolytes, respectively^{21–23}. The voltage increased substantially due to the more negative potential of the Zn reaction in alkaline-based electrolytes (-1.199 V vs. SHE)^{5,24,25}. Nevertheless, the decoupled system necessitates incorporating cation-exchange membranes (CEM), anion-exchange membranes (AEM), and a neutral buffer. This introduction substantially elevates the cost and structural intricacy of the batteries. Furthermore, constrained by the migration rate and resistance of ion transport across the membrane, the battery's rate performance and cycling capacity are markedly diminished. In short, developing catholytes with reversible MnO₂ reduction reaction (MnRR) while maintaining high voltage, capacity and long-term stability is still challenging.

Ions are usually present in a solvated form in electrolytes, and the solvation structure of the cations can be adjusted by altering the electrolyte components (e.g., cations, anions, solvents, etc.), which in turn affects the reaction kinetics and side reactions that happen at the electrode/electrolyte interphase (Figure 1c)^{26–28}. Cations, as essential constituents of the electrolyte, play a vital role in modulating the hydrogen bonding network^{29,30} or influencing the structure of MnO₂ through doping³¹ or pre-intercalation¹⁶. By employing appropriate cations, the challenge of sluggish MnRR kinetics can be potentially resolved (Figure 1c,1 and 2). However, a consensus has yet to be reached regarding the

View Article Online
DOI: 10.1039/D4EE03385J



modulation of the solvation structure of Mn^{2+} by anions, especially regarding its subsequent impact on the formation/decomposition mechanism of $\text{Mn}^{2+}/\text{MnO}_2$.

In this work, we successfully demonstrated a reversible $\text{Mn}^{2+}/\text{MnO}_2$ reaction by modulating the solvation-shell structure of Mn^{2+} and the structure of electrodeposited MnO_2 , achieved through a cation-assisted effect. The Zn-Mn FBs with Mg^{2+} exhibit an impressive high voltage of 1.91 V at 20 mA cm^{-2} and long-term stability (over 2600 cycles at 20 mA cm^{-2} , 5 mAh cm^{-2}), thus realizing a considerably high energy density of 38.2 mWh cm^{-2} in a cycle and 23.75 Wh cm^{-2} cumulatively.

Results and discussion

Electrolyte stability and structure characterization

Pure Mn-H electrolyte is made by 1M Mn salt and 0.2 M HCl in deionized water, and 4 M Mg salt is dissolved into Mn-H electrolyte to form Mn-Mg-H electrolyte. The Mn-H electrolyte is the baseline for comparing electrolyte stability and property variation. Since the reaction potential of MnO_2 is similar to the acidic OER potential ($E^0_{\text{OER}} = 1.23 \text{ V vs. SHE}$), the widening of the electrolyte window is required to improve the MnO_2 reaction reversibility. The cathodic oxidation reaction and electrolyte stability window are shown by linear scanning voltammetry (LSV) curves, and the corresponding oxygen evolution amounts in Figure 2a, where the solid lines indicate the response currents at different potentials and the dashed lines are the corresponding oxygen amount. In the Mn-H electrolyte, the onset potential of the oxidation reaction starts at 0.97 V, accompanied by a few amount of oxygen precipitation (3.7 μmol), indicating a side reaction in the oxidation of MnO_2 . When the potential increased above 1.62 V, the oxidation current rose sharply, accompanied by the amount of oxygen >100



μmol . In contrast, for the Mn-Mg-H electrolyte, there is almost no oxygen production in the interval from 0.89 V to 1.56 V. After the potential was increased to 2.2 V, only 25.9 μmol of oxygen was precipitated at most, indicating better anti-hydrolysis stability.

To understand the role of Mg^{2+} in stabilizing the Mn-based electrolytes, Fourier transform infrared (FT-IR) and Raman spectra of pure water and varied Mg^{2+} concentration in Mn-H electrolytes are collected and compared (Figure 2b, 2c and S1). According to the previous report, H_2O molecules interact with ions through hydrogen bonds³², electrostatic forces³³, and charge transfer³⁴, resulting in a hydration shell. The H-bond and vibrational characteristics of water in the solvated shell are different from those of free water in the bulk phase, so the effect of Mg^{2+} on the electrolyte H-bond network can be illustrated below: A water molecule can form a maximum of four H-bonds with other H_2O molecules by donating protons on the H atom and accepting protons through the lone pair electrons on the O atom³⁵ (Figure S2), corresponding to four different types of H-bond: DA, DAA, DDA and DDAA. The "D" and "A" are the acronyms of the H_2O molecules that donate and accept protons, respectively³⁰. These H-bonds appear as OH symmetric stretching at different positions in the Raman spectrum at ~ 3200 , 3400 and 3600 cm^{-1} for DDAA, DA and DDA, respectively³⁶. The schematic of the four different types of H-bonds is shown in Figure S3. As shown in Figure 2b, the Raman spectrum of Mn-H is similar to that of pure water, while the electrolyte with Mg^{2+} shows attenuated DDAA peaks that significantly diminish with increasing Mg^{2+} concentration. The O-H absorption at the lower frequency region ($\sim 3200 \text{ cm}^{-1}$) of the FT-IR spectra³⁷ in Figure 2c, corresponding to the strong H-bond of DDAA-related structure, shows a similar trend. These results suggest that massive Mg^{2+} in the electrolyte disrupts the original H-bond network in Mn-H electrolytes and weakens the strongly hydrogen-bonded

View Article Online
DOI: 10.1039/D4EE03385J



water.

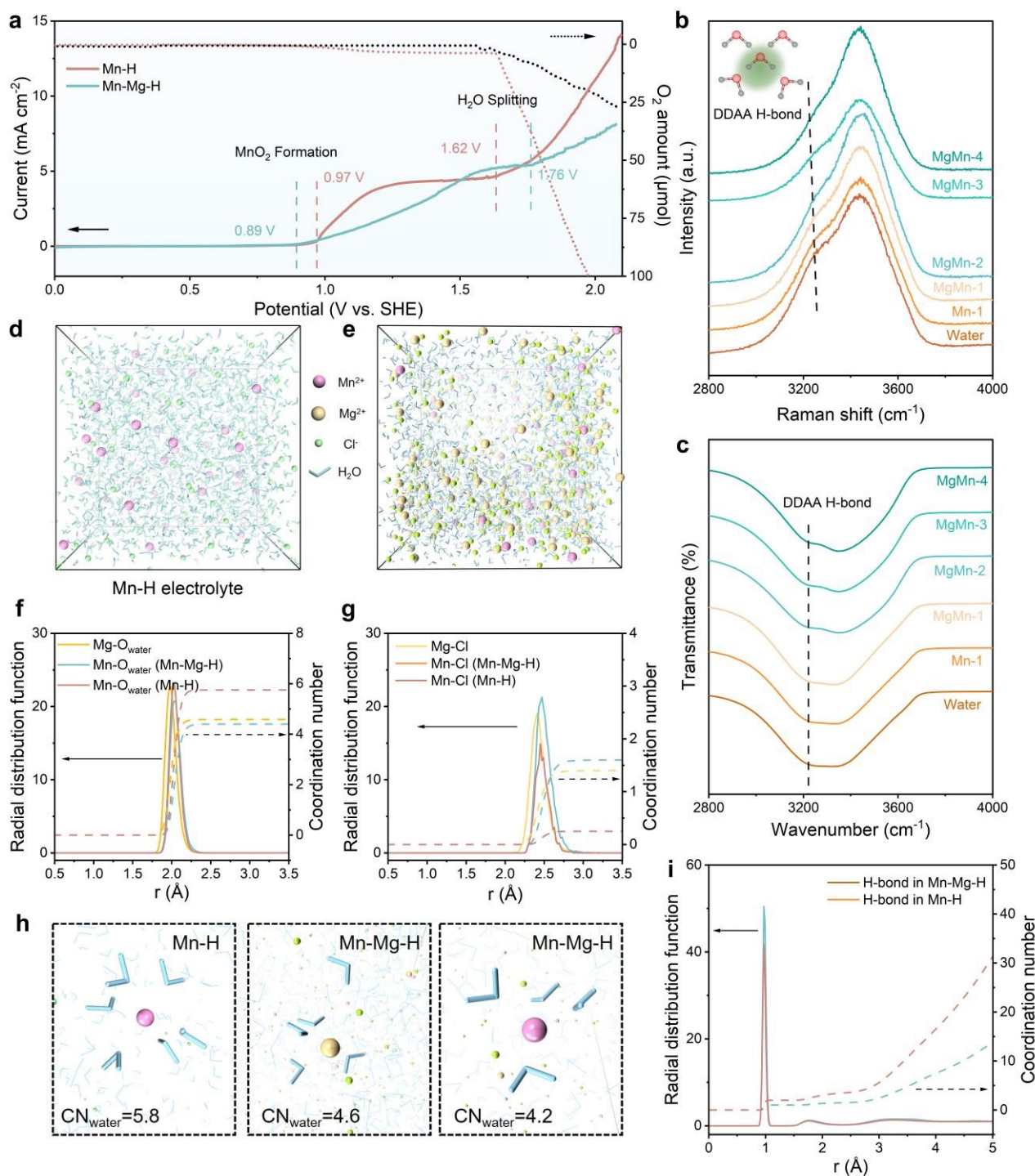


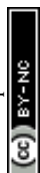
Figure 2. Stability and structure characterization of Mn-H and Mn-Mg-H electrolytes.

(a) Linear scanning voltammetry curves and the corresponding oxygen amount of Mn-H and Mn-Mg-H electrolytes in three-electrode cells at 1 mV s^{-1} . The working electrode is carbon felt, with a counter and reference electrode of Pt plate and Ag/AgCl, respectively. (b) Raman and (c) FT-IR spectra of



water, Mn-H and Mn- x Mg-H ($x=1, 2, 3, 4$ M). The inset image of (b) shows the strong H-bond with DDAA type. Snapshot of (d) Mn-H and (e) Mn-Mg-H from MD simulations. (f) The radial distribution functions and coordination number of cation- O_{water} . (g) The radial distribution functions and coordination number of cation- Cl^- . (h) The visualized solvation structures of Mn^{2+} and Mg^{2+} in Mn-H and Mn-Mg-H. (i) The radial distribution functions of water molecules.

To further classify the effect of Mg^{2+} on the structure of H-bond and the solvation structure of Mn^{2+} , which is crucial to improving the electrolyte stability, classical molecular dynamics (MD) simulations for Mn-H and Mn-Mg-H were performed. Each model contains 2000 water molecules and a corresponding number of ions. The snapshots of the electrolytes with MD simulation in Figures 2d and 2e show a large amount of free water uniformly dispersed in Mn-H. In contrast, in Mn-Mg-H, water molecules are enriched near the cations. The radial distribution functions (RDF) of cation- O_{w} (oxygen in H_2O) as well as cation- Cl^- are analyzed concerning the apparent coordination number (CN), as shown in Figures 2f, 2g and S4. In Figure 2f, the peak of RDF defines the radius of the first hydration shell. In the Mn-Mg-H electrolyte, the distance between Mg^{2+} and O_{w} ($\approx 1.97 \text{ \AA}$) is closer than Mn^{2+} - O_{w} ($\approx 2.07 \text{ \AA}$). This value ($\approx 2.07 \text{ \AA}$) is also slightly larger than the distance of Mn^{2+} - O_{w} in Mn-H ($\approx 2.03 \text{ \AA}$), and the presence of Mg^{2+} weakens the RDF peak of Mn^{2+} - O_{w} . These results indicate that water is more tightly bound to Mg^{2+} than Mn^{2+} , and the hydration shell of Mn^{2+} is loosened thanks to the addition of Mg^{2+} , which is attributed to the higher charge density of Mg^{2+} . Moreover, more Cl^- bound to Mn^{2+} and enters the first solvation sheath of Mn^{2+} due to adding MgCl_2 , further reducing the H_2O around Mn^{2+} (Figures 2g). The visualized solvation structures of Mn^{2+} and Mg^{2+} are shown in Figure 2h. The Mn-H electrolyte has 5.8 H_2O molecules and 0.25 Cl^- in the first solvation shell Mn^{2+} . The number of H_2O decreases to 4.2, and Cl^- increases to 1.6 in the solvation sheath of Mn^{2+} after adding



4M MgCl₂. The aggregation of water molecules by Mg²⁺ effectively reduces the H₂O amount in the Mn²⁺ solvation layer and breaks the H-bond structure in Mn-H (Figure 2i). The average number of H-bonds in the first (R₁≈0.97 Å) and second (R₂≈1.75 Å) hydration layer of water molecules is reduced from 2 and 3.5 to 1 and 1.5, respectively. Enabled by the high charge density of Mg²⁺ in the electrolyte, the amount of free and Mn-solvated water is decreased, which effectively elevates the electrolyte stability at high voltage and suppresses oxygen evolution side reactions (OER) during MnO₂ deposition.

Reaction kinetics and reversibility of MnO₂ formation/decomposition

In order to study the effect of Mg²⁺ on the reaction behavior of MnO₂, the cyclic voltammetry (CV) behavior of Mn-H and Mn-Mg-H is investigated in the three-electrode system, as shown in Figure 3a. Since the MnO₂ cathode undergoes two types of reactions, deposition/dissolution and intercalation, at different potentials, an additional 0.5 M ZnCl₂ was added to clarify the effect of MnO₂ accumulation on the cathodic reaction. It can be observed that the Mn²⁺ oxidation and MnRR occur mainly at the potential above 1.2 V, with an onset oxidation potential of 1.27 V and reduction peak at 1.25 V, corresponding to the formation and decomposition of MnO₂, respectively. The formed MnO₂ powder can be observed to diffuse rapidly from the cathode surface into bulk electrolytes (Figure S5a and S5b), leading to the corresponding CV curves in which the reduction current is much smaller than the oxidation current (Figure 3a). As for the Mn-H system, a completely different reaction behavior is exhibited. Mn²⁺ is oxidized to form MnO₂ in the first positive sweep without MnO₂ particles escaping from the catholyte, which remains transparent (Figure S5c).



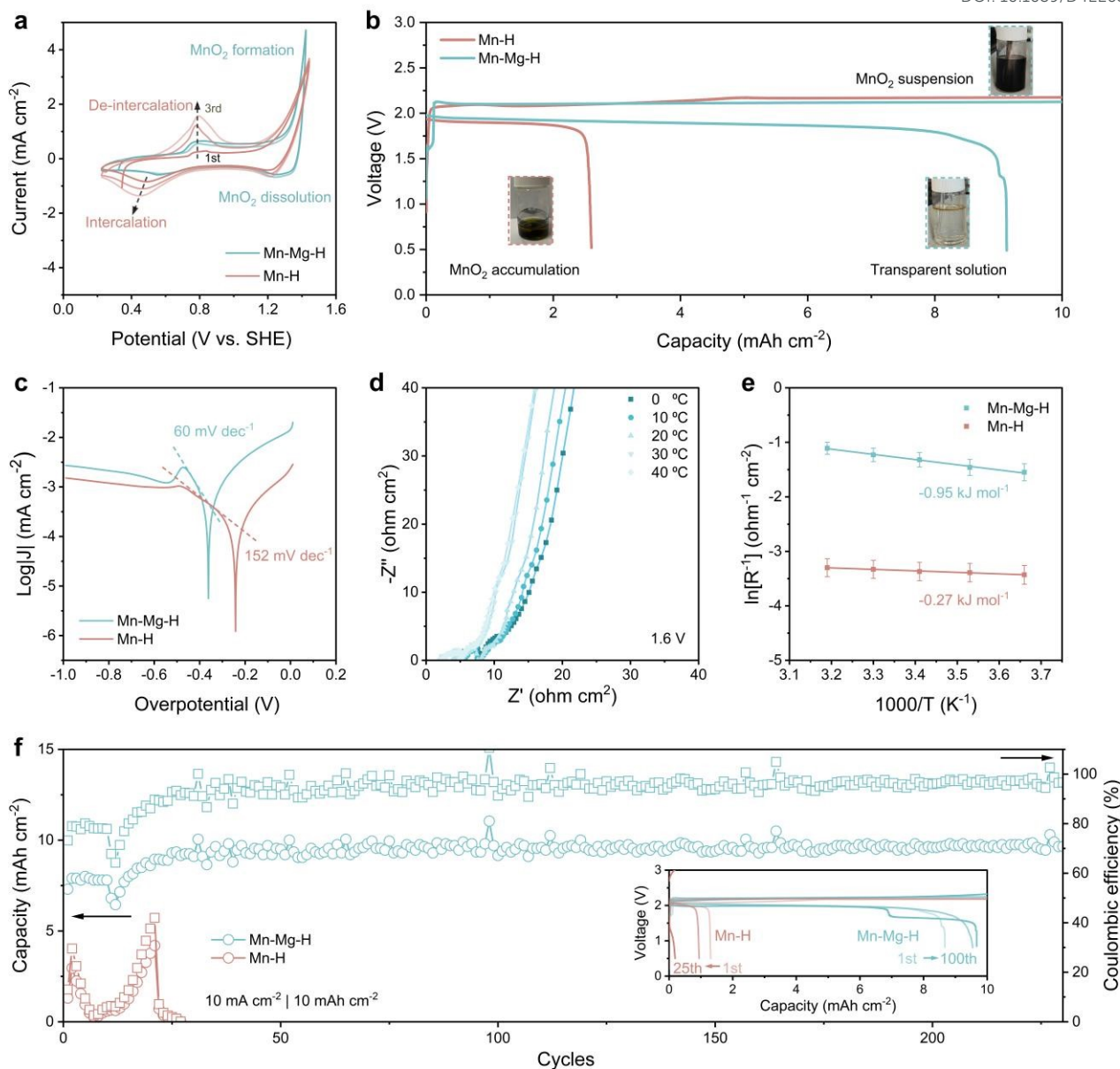


Figure 3. Electrochemical performance of Mn-based reaction in Mn-H and Mn-Mg-H electrolytes.

(a) Cyclic voltammograms for the first three cycles of Mn-H and Mn-Mg-H electrolyte in three-electrode cell at 1 mV s^{-1} . The working electrode is carbon felt, with a counter and reference electrode of Pt plate and Ag/AgCl, respectively. (b) Initial galvanostatic charge and discharge (GCD) profiles of Zn-Mn FBs with the current density of 5 mA cm^{-2} in both electrolytes. The inset optical photos are the electrolytes at different states of charge. (c) Tafel plots of the MnRR. (d) Nyquist plot of Zn-Mn flow battery with Mn-Mg-H electrolyte from $0 \text{ }^\circ\text{C}$ to $40 \text{ }^\circ\text{C}$ at the constant voltage of 1.6 V to ensure MnRR



occurs. (e) Arrhenius fitted curves of R_{ct} vs. temperature in Mn-H and Mn-Mg-H based Zn-Mn flow batteries. (f) Cycle performance of Mn-H and Mn-Mg-H based Zn-Mn FBs at 10 mA cm^{-2} with a cut-off capacity of 10 mAh cm^{-2} . The inset shows the GCD curves corresponding to different cycles.

In contrast, the reduction current corresponding to the decomposition of MnO_2 is much smaller than that at oxidation (Figure 3a), and the reduction potential is more negative (1.20 V) compared to 1.25 V, which indicates the poorer reversibility of the MnRR in Mn-H electrolyte. Moreover, in the following scanning process toward lower potentials, the cathode in the Mn-H system shows a pronounced reduction peak at 0.48 V and an emerging oxidation peak at 0.76 V in the second positive scanning, which is sharper with the increase of cycling. This redox behavior corresponds to the cation intercalation/de-intercalation process of the MnO_2 electrode, indicating that the MnO_2 deposition/dissolution process can hardly occur in the Mn-H system. The accumulation of MnO_2 on the cathode induces undesired electrochemical processes.

Different electrochemical behaviors lead to significant differences in battery performance, verified by assembling the Zn-Mn FBs (Figure S6). To mitigate the potential interference of Zn^{2+} on the MnO_2 reaction, as discussed earlier, a cation exchange membrane is employed to separate the cathodic and anodic chambers. Mn-H and Mn-Mg-H are utilized as the catholyte, respectively, while 2M ZnCl_2 with acetate buffer pair is used as anolyte. In Figure 3b, the initial charge voltage of both batteries exceeds 2.0 V, and the catholyte of Mn-Mg-H becomes progressively darker as the charge depth increases due to the MnO_2 products being washed into the reservoir by the electrolyte flow. In the following discharge process, the Mn-H-based battery terminates at 2.6 mAh cm^{-2} , with some black residual in the reservoir. In comparison, the discharge plateau of Mn-Mg-H-based flow battery reaches 1.91 V in



Figure 3b, with the initial Coulombic efficiency (CE) significantly elevated from 26% (in Mn-H) to 91%. The produced MnO_2 in Mn-Mg-H catholytes almost wholly decomposed at the end of the discharge, and the electrolyte becomes clear again (inset photo of Figure 3b). The low capacity of Mn-H-based battery is caused by the sluggish kinetics of MnRR, as evidenced by the Tafel plots in Figure 3c. Tafel slope indicates the required overpotential for increasing the reaction current, which is 152 mV dec^{-1} for Mn-H compared to 60 mV dec^{-1} for Mn-Mg-H. As for the lower temperature with a poorer mass transfer, the gap between the two electrolytes is even more pronounced. At 0°C (Figure S7), the Tafel slope of Mn-Mg-H (83 mV dec^{-1}) is much smaller than that of the Mn-H electrolytes (227 mV dec^{-1}). The temperature dynamic electrochemical impedance spectra (EIS) at a constant voltage of 1.6 V and the corresponding equivalent circuit are shown in Figures 3d and S8. The variation of the reaction resistance (R_{ct}) with temperature was fitted according to the Arrhenius equation, which led to the apparent activation energy (E_a) of MnRR, as shown in Figure 3e. The E_a of Mn-Mg-H is $-0.95 \text{ kJ mol}^{-1}$ compared to -0.27 in Mn-H, illustrating that MnRR occurs in both electrolytes at 1.6 V with the faster kinetics in Mn-Mg-H-based battery. Superior kinetics bring significantly improved reversibility, reflected in the cycling performance shown in Figure 3f. The discharge capacity of Mn-Mg-H-based flow batteries maintains stably at $\sim 9.5 \text{ mAh cm}^{-2}$ for over 250 cycles. In comparison, the capacity of Mn-H-based batteries decays dramatically in the initial several cycles due to the difficulty of decomposing MnO_2 products.

Reduced crystallinity of Mg-doped MnO_2 enabling reversible MnRR



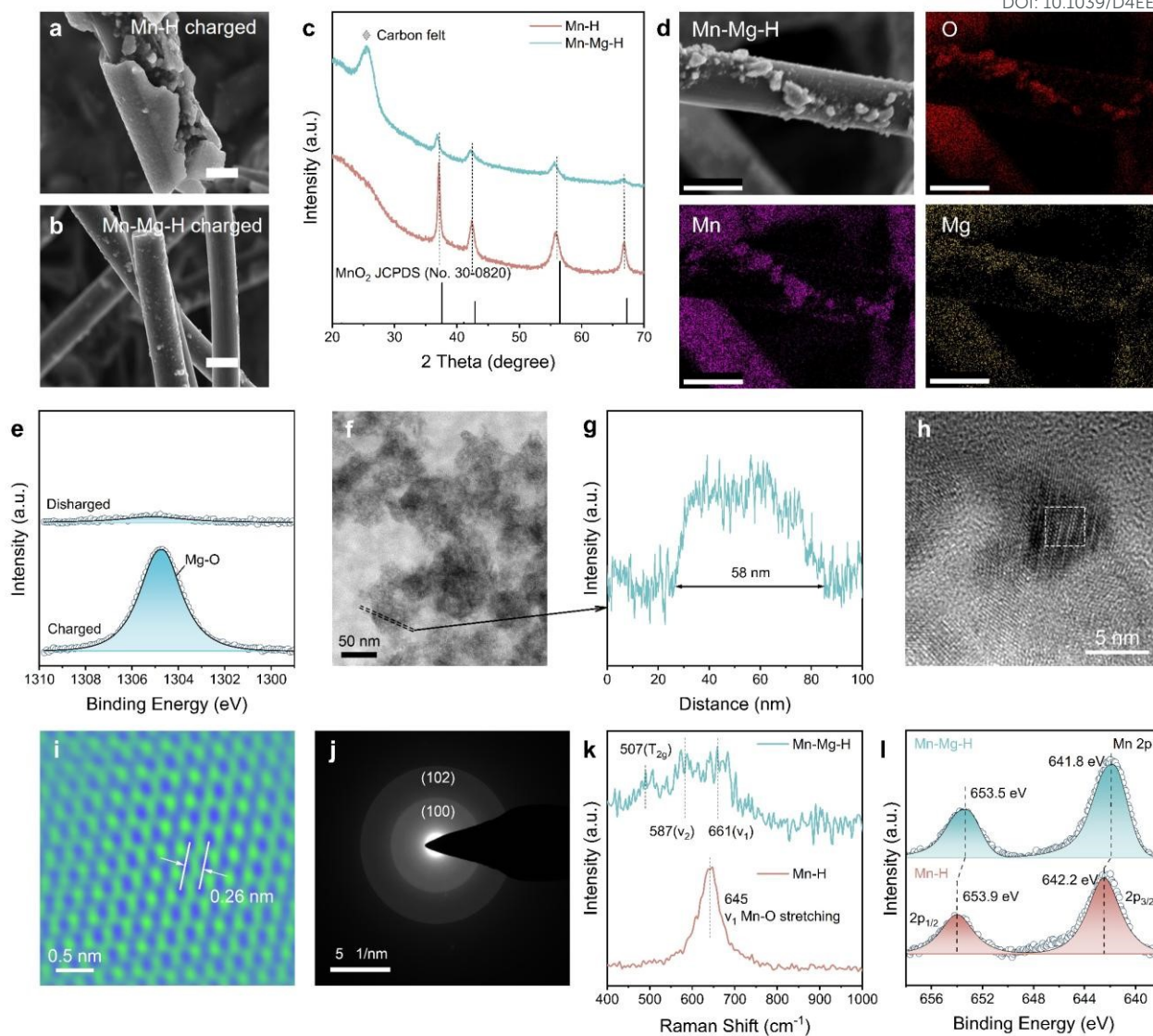


Figure 4. Structure characterization of MnO₂ products.

Scanning electron microscope (SEM) images of MnO₂ products in (a) Mn-H and (b) Mn-Mg-H electrolytes, respectively. The scale bar is uniformly 10 μm . (c) XRD patterns of the discharged cathodes. (d) Energy dispersive spectrometer (EDS) mapping of MnO₂ in Mn-Mg-H. The scale bar is uniformly 10 μm . (e) Mg 1s XPS spectra of charged and discharged Mn-Mg-H cathode. (f) TEM image of MnO₂ products in Mn-Mg-H. The area enclosed by dashed line corresponds to (g) the thickness profile. (h) HRTEM image of MnO₂ products in Mn-Mg-H. (i) Atomic resolution TEM image of the white dashed area in Fig. 4g. (j) SAED of MnO₂ in Mn-Mg-H. (k) Raman spectra of electrodeposited MnO₂ in Mn-Mg-H and Mn-H electrolytes. (l) Mn 2p XPS spectra of charged Mn-H and Mn-Mg-H cathode.



Characterizing the composition and structure of the products can help figure out the mechanism of the irreversible MnO₂ reaction in the Mn-H electrolytes. In Figure 4a, charging products in the Mn-H electrolyte are attached to the surface of carbon fiber (CF) and aggregates on the cathode (Figure S9a). Nevertheless, only fine micron-sized particles (2~5 μm) are deposited on the CF in Mn-Mg-H-based battery (Figure 4b), and the cathode remains fresh (Figure S9b), which is also echoed by the observation of rapid blackening of electrolytes mentioned in Figure 3b. X-ray diffraction patterns in Figure 4c show that the charged products in both electrolytes are γ-MnO₂ but with better crystallinity in the Mn-H electrolyte. Considering the low electrical conductivity of MnO₂ (~10⁻⁶ S cm⁻¹ at room temperature)³⁸, and the fact that high crystallinity implies high stability of the bulk phase, it is not surprising that MnO₂ is difficult to decompose in Mn-H electrolyte (Figure S10 and S11).

Notably, the (100) and (102) peaks of MnO₂ in Mn-Mg-H are slightly shifted to a lower angle, and the structural variations are responsible for the differences in the deposition patterns. The EDS mapping, through SEM (Figure 4d and S12), high angle annular dark field-scanning transmission electron microscopy (HAADF-STEM, Figure S13 and Table S1) and the X-ray photoelectron spectroscopy (XPS) spectra of charged/discharged cathodes (Figures 4e and S14) demonstrate the existence of Mg-doping in MnO₂. The exact amount of Mg²⁺ was further determined by the Inductively Coupled Plasma Mass Spectrometry (ICP-MS), and its relative elemental ratio to Mn²⁺ was 0.015:0.985 (Table S2). The structure of Mg-doped MnO₂ was further characterized by transmission electron microscope (TEM), Raman and XPS in Figures 4f-4l. The diameter of fully dispersed particles is ~58 nm, as shown in Figures 4f and 4g. The High-resolution TEM (HRTEM) in Figures 4h and 4i illustrates the lattice spacing of (100) facet $d_{(100)}$ is increased from 2.42 to 2.60 Å by Mg-doping. This



result is also consistent with the diameter of the (100) diffraction ring in the selected area of electron diffraction (SAED) (Figure 4j). Raman spectra in Figure 4k show the structural differences between MnO₂ and Mg-doped MnO₂. The γ -MnO₂ can be viewed as an intergrowth of pyrolusite and ramsdellite, and the defects depend on the relative ratio and arrangement of both structures³⁹. The Raman spectrum of Mn-H displays a distinct peak at approximately 645 cm⁻¹, indicative of MnO₆ octahedra stretching mode. In Mg-doped MnO₂ (Figures 4k and S15), three subtle peaks at around 507, 587, and 661 cm⁻¹ suggest a rise in pyrolusite defects within the ramsdellite structure. This increase in defects leads to a heightened electron density around the Mn centers, confirmed by the downshift in the binding energy of the Mn 2p peaks in the XPS spectra, as shown in Figure 4l, S14 and S16. In the Mn-Mg-H catholytes, Mg doping in electrodeposited MnO₂ results in expanded atomic spacing and increased defects. These alterations define the structure and morphology of MnO₂ products, promoting the formation of more dispersed secondary MnO₂ particles in the catholyte prevents the buildup of a passivating layer on the electrode surface, which are pivotal in substantially improving the kinetics of the MnRR.

Battery performance of Mn-Mg-H-based Zn-Mn FBs

The enhanced MnRR kinetics notably boost both the rate and cycling performance of the Zn-Mn flow batteries. As shown in Figure 5a, the Zn-Mn FBs with Nafion membrane exhibit exceptional rate performance and reversibility at 10 mAh cm⁻². The corresponding voltage profiles of Zn-Mn FBs at various rates are shown in Figure 5b. After potentiostatic charged at 2.2 V, the discharge voltage reached 2.0, 1.97, 1.91, 1.69 and 1.21 V at 10, 15, 20, 30 and 40 mA cm⁻², respectively. Specifically, the 1.91 V platform is the highest voltage reported for Zn-Mn FBs over 20 mA cm⁻². Meanwhile, the



CE of Zn-Mn FBs maintains stable around 90% from 10 mA cm⁻² to 40 mA cm⁻². After switching to the initial current density of 10 mA cm⁻², the voltage of Zn-Mn FBs is reinstated to 1.98 V, indicating excellent reversibility at high current densities. Furthermore, owing to the improved reversibility and high voltage, the Zn-Mn FBs deliver the highest power density of 52.71 mW cm⁻² at 35 mA cm⁻² from 10 to 50 mA cm⁻² (Figure 5c).

View Article Online
DOI: 10.1039/D4EE03385J

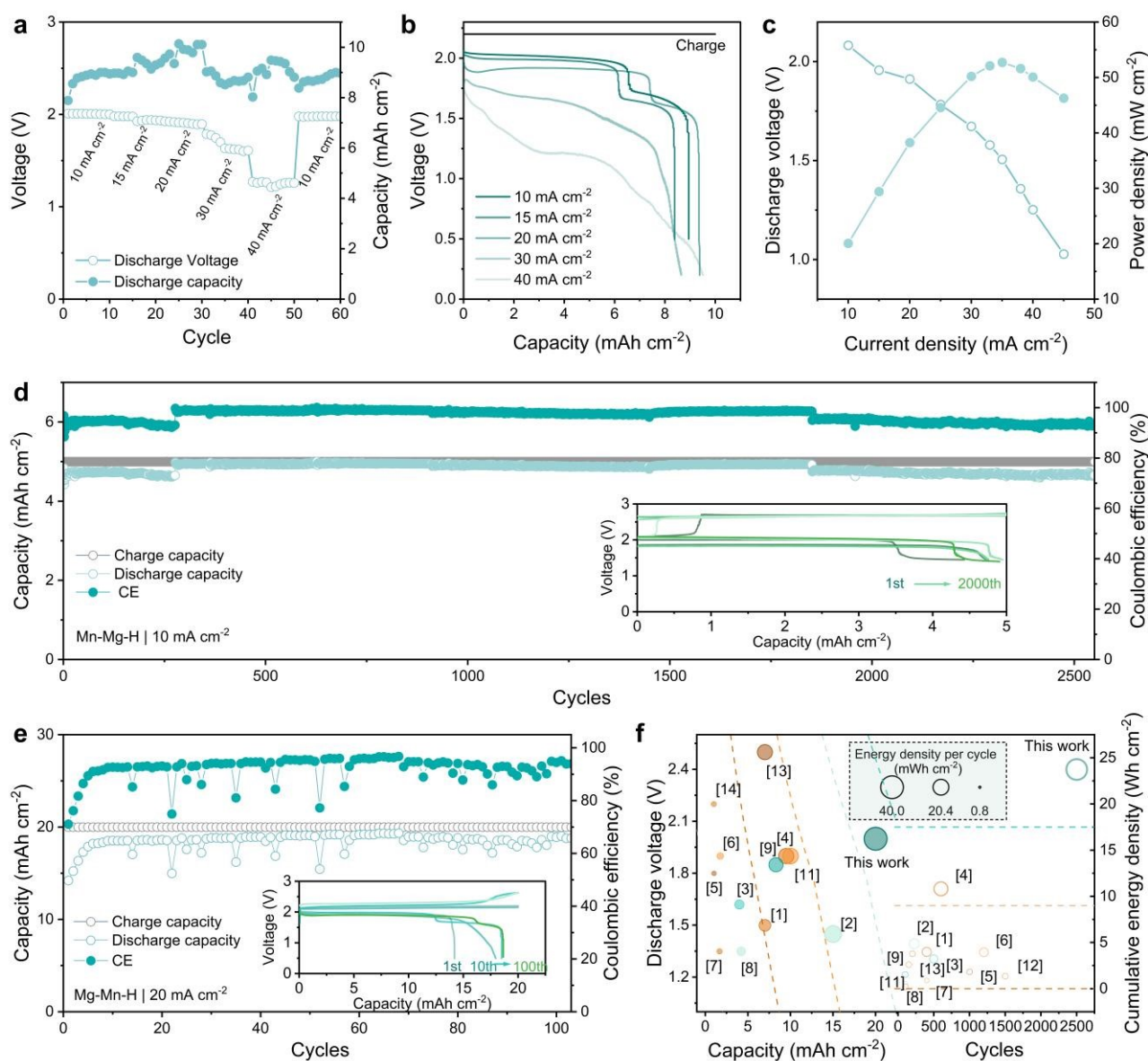


Figure 5. Performance of Zn-Mn FBs with Mn-Mg-H based electrolyte.

(a) Rate performance at a constant charging cut-off capacity of 10 mAh cm⁻². (b) Voltage-capacity



profiles at different current densities. (c) Polarization curve and power density of the flow battery. (d) Long-term cycle performance at 10 mA cm^{-2} , 5 mAh cm^{-2} . The inset graph exhibits voltage profiles at different cycles. (e) The cycling performance of the flow battery at 20 mA cm^{-2} , 20 mAh cm^{-2} with the inset graph shows the corresponding GCD profiles. (f) Performance comparison of Zn-Mn FBs based on discharge voltage (y-axis) and areal capacity (x-axis). The noted number in Fig. 5f corresponds to the reference; only the batteries over 100 cycles are selected for comparison.

Batteries employing Mn-Mg-H electrolytes demonstrate remarkable long-term cycle stability. As illustrated in Figure 5d, when operating with a cut-off capacity of 5 mAh cm^{-2} at 10 mA cm^{-2} , the flow battery consistently performs over 2600 cycles with a high CE of over 95% while maintaining a discharge voltage above 1.90 V. The low-potential plateau ($\sim 1.5 \text{ V}$) that gradually becomes apparent with cycling may be related to the proton intercalation behavior triggered by the accumulation of a few amounts of MnO_2 , which, together with the zinc corrosion on the negative side, also contributes to the failure of the batteries (Figure S17-19, Table S3). In addition, as shown in Figure 5e, when operating at tighter conditions of higher capacity (20 mAh cm^{-2}) and elevated current density (20 mA cm^{-2}), the Zn-Mn FBs still exhibit superior cycling stability for over 100 cycles (CE $\sim 94\%$). The inset graph of GCD profiles in Figure 5e shows the settled voltage platform at 1.90 V, suggesting the outstanding reversibility of $\text{Mn}^{2+}/\text{MnO}_2$ conversion reaction. Additionally, thanks to the Mn-Mg-H electrolyte with reduced H-bond strength, it is operable over a wider temperature range. The Mn-Mg-H based Zn-Mn FBs maintained stability for 100 cycles at both 80°C and 0°C (Figure S20), exhibiting considerable resistance to temperature fluctuation. The voltage, capacity and stability improvements contribute to the energy density of Zn-Mn FBs. The performance of reported Zn-Mn FBs in recent years has been meticulously cataloged, with a particular emphasis on their energy density. This comprehensive



evaluation is illustrated in Figure 5f and detailed in Table S3, highlighting significant advancements in this domain. The Zn-Mn FBs utilizing Mn-Mg-H catholytes present noticeably high energy density (38.2 mWh cm⁻² per cycle and 23.75 Wh cm⁻² cumulatively). Such exceptional performance demonstrates the effectiveness of improving the reversibility of the MnO₂ conversion reaction through the dual function of intense hydration and doping of Mg²⁺.

Conclusion

In summary, we demonstrated the cation-assisted Mn²⁺/MnO₂ reaction with significantly improved MnO₂ reduction reaction (MnRR) kinetics, enabling high voltage and long-term stable Zn-Mn FBs. FT-IR, Raman and MD simulations showed the vigorous hydration of Mg²⁺ to enhance the electrolyte stability upon MnO₂ deposition above 2.0 V. The Mg-doped MnO₂ characterized by EDS, HR-TEM and XPS spectra contain more structural defects and larger atomic spacing, which was easier to decompose and disperse in catholyte, avoiding the cathode passivation due to MnO₂ aggregation. The Mg²⁺-regulated Zn-Mn FBs realize a high discharge voltage above 1.91 V at 20 mA cm⁻², and superior cycling stability for over 2600 cycles at 5 mAh cm⁻² (10 mA cm⁻²) and 100 cycles at 20 mAh cm⁻² (20 mA cm⁻²), an exceptional energy density of 38.2 mWh cm⁻² per cycle and 23.75 Wh cm⁻² cumulatively is realized. Our research demonstrates a novel approach to enhancing the performance of Zn-Mn FBs through electrolyte engineering. This approach offers a viable strategy for developing scalable energy storage devices with high power and energy density suitable for practical applications.

View Article Online
DOI: 10.1039/D4EE03385J



Acknowledgement

This work is partially supported by a grant from Shenzhen Science and Technology Program (SGDX20211123151002003) and Innovation and Technology Fund (GHP/191/21SZ).



Reference

- Z. Zhao, X. Liu, M. Zhang, L. Zhang, C. Zhang, X. Li and G. Yu, *Chem. Soc. Rev.*, 2023, 10.1039/D2CS00765G.
- F. Ai, Z. Wang, N.-C. Lai, Q. Zou, Z. Liang and Y.-C. Lu, *Nat Energy*, 2022, **7**, 417–426.
- S. Wang, T. Li, Y. Yin, N. Chang, H. Zhang and X. Li, *Nano Energy*, 2022, **96**, 107120.
- H. Pan, Y. Shao, P. Yan, Y. Cheng, K. S. Han, Z. Nie, C. Wang, J. Yang, X. Li, P. Bhattacharya, K. T. Mueller and J. Liu, *Nat Energy*, 2016, **1**, 1–7.
- C. Zhong, B. Liu, J. Ding, X. Liu, Y. Zhong, Y. Li, C. Sun, X. Han, Y. Deng, N. Zhao and W. Hu, *Nat Energy*, 2020, **5**, 440–449.
- S. Wang, Z. Wang, Y. Yin, T. Li, N. Chang, F. Fan, H. Zhang and X. Li, *Energy & Environmental Science*, 2021, **14**, 4077–4084.
- G. Li, W. Chen, H. Zhang, Y. Gong, F. Shi, J. Wang, R. Zhang, G. Chen, Y. Jin, T. Wu, Z. Tang and Y. Cui, *Adv. Energy Mater.*, 2020, **10**, 1902085.
- N. Liu, M. K. J. Pan, Y. Hu, Y. Sun and X. Liu, *J. Electrochem. Soc.*, 2020, **167**, 040517.
- C. Xie, T. Li, C. Deng, Y. Song, H. Zhang and X. Li, *Energy Environ. Sci.*, 2020, **13**, 135–143.
- X. Yu, Y. Song and A. Tang, *Journal of Power Sources*, 2021, **507**, 230295.
- J. Lei, Y. Yao, Z. Wang and Y.-C. Lu, *Energy & Environmental Science*, 2021, **14**, 4418–4426.
- W. Xiang, M. Yang, M. Ding, X. Chen, J. Liu, G. Zhou, C. Jia and G. I. N. Waterhouse, *Energy Storage Materials*, 2023, **61**, 102894.
- G. Liang, F. Mo, H. Li, Z. Tang, Z. Liu, D. Wang, Q. Yang, L. Ma and C. Zhi, *Advanced Energy Materials*, 2019, **9**, 1901838.
- D. Chao, W. Zhou, C. Ye, Q. Zhang, Y. Chen, L. Gu, K. Davey and S. Qiao, *Angew. Chem. Int. Ed.*, 2019, **58**, 7823–7828.
- X. Guo, J. Zhou, C. Bai, X. Li, G. Fang and S. Liang, *Materials Today Energy*, 2020, **16**, 100396.
- H. Yang, W. Zhou, D. Chen, J. Liu, Z. Yuan, M. Lu, L. Shen, V. Shulga, W. Han and D. Chao, *Energy & Environmental Science*, 2022, **15**, 1106–1118.
- X. Zeng, J. Liu, J. Mao, J. Hao, Z. Wang, S. Zhou, C. D. Ling and Z. Guo, *Advanced Energy Materials*, 2020, **10**, 1904163.
- H. Moon, K.-H. Ha, Y. Park, J. Lee, M.-S. Kwon, J. Lim, M.-H. Lee, D.-H. Kim, J. H. Choi, J.-H. Choi and K. T. Lee, *Advanced Science*, 2021, **8**, 2003714.
- Z. Liu, Y. Yang, S. Liang, B. Lu and J. Zhou, *Small Structures*, 2021, **2**, 2100119.
- J. Sun, X. Zheng, K. Li, G. Ma, T. Dai, B. Ban, Y. Yuan, M. Wang, M. Chuai, Y. Xu, Z. Liu, T. Jiang, Z. Zhu, J. Chen, H. Hu and W. Chen, *Energy Storage Materials*, 2023, **54**, 570–578.
- B. Kim, Y. S. Kim, D. Dulyawat and C.-H. Chung, *Journal of Energy Storage*, 2023, **72**, 108337.
- D. Chao, C. Ye, F. Xie, W. Zhou, Q. Zhang, Q. Gu, K. Davey, L. Gu and S.-Z. Qiao, *Advanced Materials*, 2020, **32**, 2001894.
- C. Liu, X. Chi, Q. Han and Y. Liu, *Advanced Energy Materials*, 2020, **10**, 1903589.
- Y. Zhu, Y. Cui, Z. Xie, Z. Zhuang, G. Huang and X. Zhang, *Nat Rev Chem*, 2022, **6**, 505–517.
- S. Wang, C. Yuan, N. Chang, Y. Song, H. Zhang, Y. Yin and X. Li, *Science Bulletin*, 2021, **66**, 889–896.
- D. Wu, L. M. Housel, S. T. King, Z. R. Mansley, N. Sadique, Y. Zhu, L. Ma, S. N. Ehrlich, H. Zhong,



- E. S. Takeuchi, A. C. Marschilok, D. C. Bock, L. Wang and K. J. Takeuchi, *J. Am. Chem. Soc.*, 2022, **144**, 23405–23420. View Article Online
DOI:10.1039/D4EE03385J
- 27 H. Chen, C. Dai, F. Xiao, Q. Yang, S. Cai, M. Xu, H. J. Fan and S.-J. Bao, *Advanced Materials*, 2022, **34**, 2109092.
- 28 Y. Deng, H. Wang, M. Fan, B. Zhan, L.-J. Zuo, C. Chen and L. Yan, *J. Am. Chem. Soc.*, DOI:10.1021/jacs.3c07764.
- 29 U. T. D. Huynh, A. Lerbret, F. Neiers, O. Chambin and A. Assifaoui, *J. Phys. Chem. B*, 2016, **120**, 1021–1032.
- 30 J. Liu, D. Dong, A. L. Caro, N. S. Andreas, Z. Li, Y. Qin, D. Bedrov and T. Gao, *ACS Cent. Sci.*, 2022, **8**, 729–740.
- 31 Q. Wang, W. Zhou, Y. Zhang, H. Jin, X. Li, T. Zhang, B. Wang, R. Zhao, J. Zhang, W. Li, Y. Qiao, C. Jia, D. Zhao and D. Chao, *Environ Chem Lett*, 2018, **16**, 683–694.
- 32 H. Xu and B. J. Berne, *J. Phys. Chem. B*, 2001, **105**, 11929–11932.
- 33 J. Åqvist and T. Hansson, *J. Phys. Chem.*, 1996, **100**, 9512–9521.
- 34 R. Laenen, T. Roth and A. Laubereau, *Phys. Rev. Lett.*, 2000, **85**, 50–53.
- 35 A. Luzar and D. Chandler, *Nature*, 1996, **379**, 55–57.
- 36 Q. Sun, *Vibrational Spectroscopy*, 2009, **51**, 213–217.
- 37 H.-C. Chen, F.-D. Mai, K.-H. Yang, L.-Y. Chen, C.-P. Yang and Y.-C. Liu, *Anal. Chem.*, 2015, **87**, 808–815.
- 38 J.-G. Wang, in *Supercapacitor Design and Applications*, IntechOpen, 2016.
- 39 C. Julien, M. Massot, S. Rangan, M. Lemal and D. Guyomard, *J Raman Spectroscopy*, 2002, **33**, 223–228.



Data availability statement

All datasets generated or analyzed during this study are included in the paper and Supplementary Information.

